buildings

MDPI

Article

Torsional Behavior of Pylon Columns with Edge Cracks in Suspension Bridges Under Wind Loads

Nan Liu [1], Jianjun Guo [2], Kunpeng Zhao [1,*], Chunyu Wang [2], Qinxi Dong [1], Xidong Yuan [2], Hui Yang [2] and Lu Zhao [1]

[1] School of Transportation Civil Engineering, Shandong Jiaotong University, Changqing University Science Park, No. 5001, Haitang Road, Jinan 250357, China; 204040@sdjtu.edu.cn (N.L.); 204041@sdjtu.edu.cn (Q.D.); 211106@sdjtu.edu.cn (L.Z.)

[2] Weihai Municipal Road Development and Management Center, No. 20, Dongshan Road, Weihai 264200, China; glzxrskb02@wh.shandong.cn (J.G.); glzxrskb01@wh.shandong.cn (C.W.)

* Correspondence: 204085@sdjtu.edu.cn; Tel.: +86-15854134206

Abstract

Cracks inevitably develop in the pylon structures of suspension bridges due to external forces such as wind loads. Cracks are a primary cause of torsional damage to the key supporting structures of suspension bridges. Therefore, torsional fracture analyses are vitally important for evaluating the safety of bridge structures. In this study, we simplified the tower structure of a suspension bridge as a homogenous cylinder. We then employed the boundary integral equations for a cylinder with edge cracks to investigate the singularity features at the crack tip. The boundary element-based method was subsequently used to divide the boundary into several elements, and different interpolation functions were adopted to compute the stress intensity factor at the crack tip. Torsional stiffness and stress intensity factor calculations were conducted for cylinders with straight and polyline edge cracks. The results were compared with the results reported in the existing literature, and the accuracy and reliability of the calculation method were validated. Finally, the numerical simulation of the torsional fracture behavior of cylinders with edge cracks under various wind loads was conducted. The maximum allowable crack lengths of a cylinder under different wind grades were acquired, further demonstrating the feasibility and practicality of the boundary element calculation method for practical applications in bridge engineering.

Keywords: torsion; fracture; boundary integral equation; cracks; bridges

1. Introduction

Suspension bridge pylons are critical load-bearing components whose mechanical performance directly governs the overall load-carrying capacity and operational safety of a bridge. Wind load is the dominant environmental load for bridges constructed in marine and open areas throughout their service life; sustained wind excitation not only induces dynamic responses in pylons, but it also triggers cumulative damage and crack formation [1]. Once edge cracks appear in pylons, their structural mechanical properties begin to significantly degrade; furthermore, the wind-induced torsional responses of pylons lead to the concentration of stress at crack tips, which accelerates crack propagation and ultimately results in torsional fracture, posing a severe threat to bridge safety [2]. Therefore, in-depth investigations into the torsional fracture mechanism of edge-cracked pylon cylinders under wind loads are of great importance for bridge safety assessment, as well as for operational and maintenance decision-making.

Check for updates

Academic Editor: Tarek Zayed

Received: 28 October 2025
Revised: 24 December 2025
Accepted: 25 December 2025
Published: 29 December 2025

Copyright: © 2025 by the authors. Licensee MDPI, Basel, Switzerland. This article is an open access article distributed under the terms and conditions of the Creative Commons Attribution (CC BY) license.

A comprehensive literature review was conducted focusing on four core research themes: torsion analysis of bridge structures, the fracture mechanics of cracked cylinders, engineering applications of the boundary element method (BEM), and the structural responses of bridges under wind loads. This review identified several notable research gaps. First, most existing studies on bridge torsion focus on static or seismic loads, paying less attention to pylon torsional responses under wind loads. There is also a lack of systematic understanding of the mechanism connecting wind-induced torsion and crack propagation [3–5]. Second, research on cracked cylinders is primarily confined to the material level, and as such it fails to integrate practical engineering contexts, such as pylon–wind load coupling, thereby limiting its relevance to engineering applications [6–14]. Third, in numerical simulations, despite the significant advantages of BEM in crack analysis, its application in the torsional fracture analysis of pylons under wind loads remains immature and its practicality in engineering terms has yet to be fully verified. Existing studies predominantly rely on the finite element method (FEM), which has inherent limitations in handling crack-tip singularity [15–20]. Finally, wind load-related research on bridge structural responses has paid inadequate attention to pylons, and the mechanism by which the dynamic characteristics of wind loads impact the stress and displacement fields at crack tips remains unclear, resulting in inadequate research on the wind-resistant assessment of damage to pylons [21–29].

To address these research gaps, this study takes edge-cracked pylon cylinders of suspension bridges as the research object, integrating the dynamic characteristics of wind loads to conduct theoretical analysis and numerical simulation of torsional fracture. The specific contributions of this study are as follows: (1) a simplified model of a homogeneous cylinder with a focus on edge cracks is established; (2) boundary integral equations for the torsion of cracked cylinders are constructed to clarify the singularity characteristics of crack tips; (3) a BEM-based numerical scheme is proposed and its reliability verified through comparisons with results previously reported in the literature; and (4) numerical simulations and parametric analysis of torsional fracture under different wind load conditions are performed to determine the maximum allowable crack length under various wind grades. The objectives of this study are to reveal the torsional fracture mechanism of edge-cracked pylons under various wind loads, improve the theoretical framework for bridge torsional fracture analysis, verify the practicality of BEM in engineering terms, and provide scientific and technical support for the wind-resistant design, damage detection, and operation and maintenance of pylons.

2. Basic Theory and Derivation

The mathematical theory of the boundary integral equation for edge-cracked cylinders combined with the BEM numerical calculation used in this study was developed based on the classical theoretical system of fracture mechanics and the BEM. This theory was first systematically proposed by Cruse in 1974, after which it was further refined by scholars such as Rizzo. It evolved into a classical theoretical framework to reveal the stress intensity factors (SIFs) of cracked bodies. Another crucial milestone in the development of this theory was the publication of the first monograph regarding the BEM, written by Brebbia in 1978 [30]. This work systematically elaborated on the theoretical system of the BEM, marking the official beginning of systematic research on this methodology.

2.1. Treatment of the Crack-Tip Singularity in the Torsion Problem of Cylinders with Edge Cracks

The primary focus of this study is to compute the torsion problem of cylinders with edge cracks; First, it is necessary to address the crack tip singularity of edge cracks in this section [31].

When a cylinder is in an elastic torsion state, its cross-sections rotate within their own planes while allowing free axial warping. A coordinate system was established for analysis, as shown in Figure 1. It was assumed that the cross-sections undergo rigid-body rotation; hence, the displacement of any arbitrary point within the cylinder is given by [32]:

$$u = -\alpha yz,\ v = \alpha xz,\ w = \alpha\phi(x, y), \tag{1}$$

where ϕ is the torsion function; G is the shear modulus; α is the torsion rate; and z is the position of the cross-section.

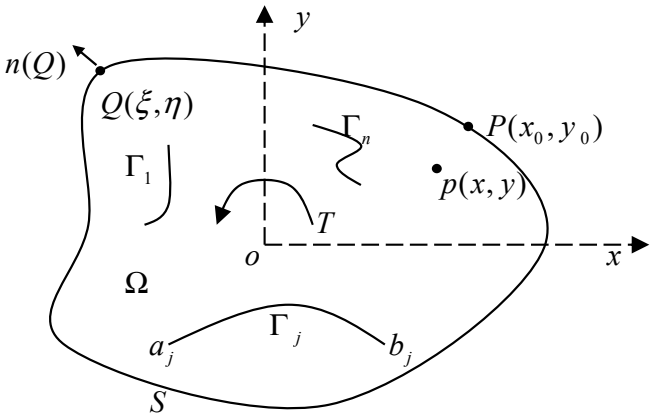


Figure 1. Cylinder with an arbitrary cross-section and arbitrary edge cracks (Note: Ω denotes the solution domain, $\Gamma_1, \ldots, \Gamma_n$ represent cracks, $n(Q)$ is the outward normal vector of domain Ω), Q (ξ,η) is a boundary element node, $p(x,y)$ is a point inside domain Ω, and $P(x_0,y_0)$ is a point on the boundary).

A local area with cracks on the boundary was examined, as illustrated in Figure 2. Local polar coordinates, i.e., (ρ, θ), at the crack tip were introduced:

$$u_\rho = 0,\ u_\theta = \alpha\rho z,\ w = \alpha\phi(\rho, \theta). \tag{2}$$

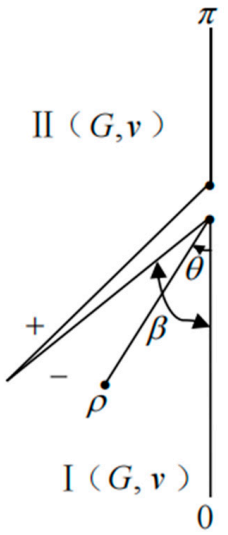


Figure 2. Coordinates of the local area at the crack (Note: I and II denote the Mode I and Mode II stress field components, respectively; θ is the polar angle, ρ is the polar radius; (G, v) represent material parameters (shear modulus, Poisson's ratio)).

Based on the geometric equation, the strain components of the particle was calculated as follows:

$$\varepsilon_r = \varepsilon_\theta = \varepsilon_z = \gamma_{r\theta} = 0,\ \gamma_{\theta z} = \frac{1}{\rho}\frac{\partial w}{\partial \theta} + \alpha\rho,\ \gamma_{\rho z} = \frac{\partial w}{\partial \rho}. \tag{3}$$

Obtained using $\nabla^2 w = 0$:

$$w = \rho^{\lambda}[A\cos(\lambda\theta) + B\sin(\lambda\theta)]. \tag{4}$$

$$\tau_{\theta z} = G\gamma_{\theta z} = G\lambda\rho^{\lambda-1}[-A\sin(\lambda\theta) + B\cos(\lambda\theta)]. \tag{5}$$

$$\gamma_{\rho z} = \lambda\rho^{\lambda-1}[A\cos(\lambda\theta) + B\sin(\lambda\theta)]. \tag{6}$$

(1) For area I $(0 < \theta < \beta)$, $(G,\ v)$:

$$w_1 = \rho^{\lambda_1}[A_1\cos(\lambda_1\theta) + B_1\sin(\lambda_1\theta)]. \tag{7}$$

$$\tau_{\theta z1} = G\gamma_{\theta z1} = G\lambda_1\rho^{\lambda_1-1}[-A_1\sin(\lambda_1\theta) + B_1\cos(\lambda_1\theta)] \tag{8}$$

$$\gamma_{\rho z1} = \lambda_1\rho^{\lambda_1-1}[A_1\cos(\lambda_1\theta) + B_1\sin(\lambda_1\theta)]. \tag{9}$$

(2) For area II $(\beta < \theta < \pi)$, $(G,\ v)$:

$$w_2 = \rho^{\lambda_2}[A_2\cos(\lambda_2\theta) + B_2\sin(\lambda_2\theta)]. \tag{10}$$

$$\tau_{\theta z2} = G\gamma_{\theta z2} = G\lambda_2\rho^{\lambda_2-1}[-A_2\sin(\lambda_2\theta) + B_2\cos(\lambda_2\theta)]. \tag{11}$$

$$\gamma_{\rho z2} = \lambda_2\rho^{\lambda_2-1}[A_2\cos(\lambda_2\theta) + B_2\sin(\lambda_2\theta)]. \tag{12}$$

Hence, the boundary between the crack $(\theta = \beta + 0, \theta = \beta - 0)$ and the surface force at the interface $(\theta = 0, \pi)$ is given by:

$$\tau_{\theta z1}|_{\theta=0} = G\lambda_1\rho^{\lambda_1-1}B_1 = 0 \tag{13}$$

$$\tau_{\theta z1}|_{\theta=\beta-0} = G\lambda_1\rho^{\lambda_1-1}[-A_1\sin(\lambda_1\beta) + B_1\cos(\lambda_1\beta)] = 0 \tag{14}$$

$$\tau_{\theta z2}|_{\theta=\beta+0} = G\lambda_2\rho^{\lambda_2-1}[-A_2\sin(\lambda_2\beta) + B_2\cos(\lambda_2\beta)] = 0 \tag{15}$$

$$\tau_{\theta z2}|_{\theta=\pi} = G\lambda_2\rho^{\lambda_2-1}[-A_2\sin(\lambda_2\pi) + B_2\cos(\lambda_2\pi)] = 0. \tag{16}$$

Equation (13) then shows that:

$$B_1 = 0. \tag{17}$$

The above equation was subsequently substituted into Equation (14) to yield:

$$A_1\sin(\lambda_1\beta) = 0. \tag{18}$$

and then,

$$\sin(\lambda_1\beta) = 0 \Rightarrow\ \ \lambda_1\beta = k\pi\ (k = 1, 2, \ldots), \tag{19}$$

where $k \leq 0$ and $\lambda_1 - 1 \leq -1$. This was then substituted into Equation (14). The distribution of the stress field was unreasonable, making it unsuitable for this situation. Thus, we used $k \geq 1$, i.e., $k = 1, 2, \ldots, n$, for the calculation. Then, to ensure that $\rho^{\lambda-1}$ approached zero at the slowest rate, we ultimately used $k = 1$. We then obtained:

$$\lambda_1 = \pi/\beta (A_1 \neq 0,\ \lambda_1 > 1). \tag{20}$$

From Equations (15) and (16), we obtained:

$$-A_2 \sin(\lambda_2 \beta) + B_2 \cos(\lambda_2 \beta) = 0. \tag{21}$$

$$-A_2 \sin(\lambda_2 \pi) + B_2 \cos(\lambda_2 \pi) = 0. \tag{22}$$

The above two equations are homogeneous linear equations, and the sufficient and necessary condition for homogeneous linear equations to have non-zero solutions is that their coefficient determinant is zero, that is:

$$-\sin(\lambda_2 \beta)\cos(\lambda_2 \pi) + \cos(\lambda_2 \beta)\sin(\lambda_2 \pi) = 0. \tag{23}$$

therefore,

$$\sin[\lambda_2(\pi - \beta)] = 0 (A_2, B_2 \neq 0, 0 < \beta < \frac{\pi}{2}) \Rightarrow \ \lambda_2(\pi - \beta) = k\pi \ (k = 1, 2, \ldots). \tag{24}$$

Similarly,

$$\lambda_2 = \pi/(\pi - \beta) (A_2, B_2 \neq 0, 0 < \beta < \frac{\pi}{2}, \ \lambda_2 > 1). \tag{25}$$

From Equations (17)–(22) and (25), we obtained:

(1) For area I ($0 < \theta < \beta$), (G, v):

$$w_1 = \rho^{\lambda_1} A_1 \cos(\lambda_1 \theta). \tag{26}$$

$$\tau_{\theta z1} = -G\lambda_1 \rho^{\lambda_1 - 1} A_1 \sin(\lambda_1 \theta). \tag{27}$$

$$\gamma_{\rho z1} = \lambda_1 \rho^{\lambda_1 - 1} A_1 \cos(\lambda_1 \theta). \tag{28}$$

where $\lambda_1 = \pi/\beta$ ($A_1 \neq 0$, $\lambda_1 > 1$).

(2) For area II ($\beta < \theta < \pi$), (G, v):

$$w_2 = \rho^{\lambda_2} C_2 \cos[\lambda_2(\theta - \beta)] \tag{29}$$

$$\tau_{\theta z2} = -G\lambda_2 \rho^{\lambda_2 - 1} C_2 \sin[\lambda_2(\theta - \beta)] \tag{30}$$

$$\gamma_{\rho z2} = \lambda_2 \rho^{\lambda_2 - 1} C_2 \cos[\lambda_2(\theta - \beta)], \tag{31}$$

where $\lambda_2 = \pi/(\pi - \beta)(A_2, B_2 \neq 0, 0 < \beta < \frac{\pi}{2}, \lambda_2 > 1)$, $C_2 = \frac{A_2}{\cos(\lambda_2 \beta)}$.

Then:

$$\left.\frac{\partial w_1}{\partial \rho}\right|_{\theta=0} = \lambda_1 A_1 \rho^{\lambda_1 - 1}, \ \left.\frac{\partial w_2}{\partial \rho}\right|_{\theta=\pi} = -\lambda_2 A_2 \rho^{\lambda_2 - 1} \frac{1}{\cos(\lambda_2 \beta)} = -\lambda_2 C_2 \rho^{\lambda_2 - 1}, \tag{32}$$

$$\left.\frac{\partial w_1}{\partial \rho}\right|_{\theta=\beta} = \lambda_1 A_1 \rho^{\lambda_1 - 1} \cos(\lambda_1 \beta) = -\lambda_1 A_1 \rho^{\lambda_1 - 1}, \tag{33}$$

$$\left.\frac{\partial w_2}{\partial \rho}\right|_{\theta=\beta} = \lambda_2 A_2 \rho^{\lambda_2 - 1} \frac{1}{\cos(\lambda_2 \beta)} = \lambda_2 C_2 \rho^{\lambda_2 - 1}, \tag{34}$$

$$\Delta w = (w_2 - w_1)|_{\theta=\beta} = \rho^{\lambda_2} A_2 \frac{1}{\cos(\lambda_2 \beta)} - \rho^{\lambda_1} A_1 \cos(\lambda_1 \beta) = 0 \Rightarrow A_2 = \rho^{\lambda_1 - \lambda_2} \cos(\lambda_1 \beta)\cos(\lambda_2 \beta) A_1 \tag{35}$$

$$\left.\frac{\partial \Delta w}{\partial \rho}\right|_{\theta=\beta} = \lambda_2 A_2 \rho^{\lambda_2 - 1} \frac{1}{\cos(\lambda_2 \beta)} - \lambda_1 A_1 \rho^{\lambda_1 - 1} \cos(\lambda_1 \beta) = \lambda_2 C_2 \rho^{\lambda_2 - 1} + \lambda_1 A_1 \rho^{\lambda_1 - 1}. \tag{36}$$

It is important that, when $\beta = \frac{\pi}{2}$, $\lambda_1 = \lambda_2 = 2$. This causes the interpolation function to be repeated on the selected different cells. To make sense of the selection of the following interpolation functions, when $\beta = \frac{\pi}{2}$, it should be assumed that $\lambda_1 = \lambda_2 = 4$, this corresponds to the eigen solution of $k = 2$.

2.2. Boundary Element Numerical Computation: Choice of an Interpolation Function

According to reference [33], the boundary integral equation can be obtained for the general torsion of a cylinder as follows:

$$\begin{aligned} &\int_{\Sigma_2} \frac{\partial \varphi(P,Q)}{\partial s(P)} F(Q) ds(Q) + \int_{\Gamma} \frac{\partial \varphi(P,Q)}{\partial s(P)} F(Q) ds(Q) \\ &+ \int_{\Sigma_2} \frac{\partial \varphi(P,Q)}{\partial s(P)} F(Q) ds(Q) - \int_{\Sigma_2} \frac{\partial \varphi(P,Q)}{\partial n(P)} q^{+}(Q) ds(Q) \\ &= -\frac{1}{2} q(P) + \int_{\Sigma} \frac{\partial \varphi(P,Q)}{\partial n(P)} q(Q) dS(Q), \end{aligned} \tag{37}$$

where $P \in S$.

$$\begin{aligned} &\int_{\Sigma_2} \frac{\partial \varphi(P,Q)}{\partial s(P)} F(Q) ds(Q) + \int_{\Gamma} \frac{\partial \varphi(P,Q)}{\partial s(P)} F(Q) ds(Q) \\ &+ \int_{S_2} \frac{\partial \varphi(P,Q)}{\partial s(P)} F(Q) ds(Q) - \int_{S_2} \frac{\partial \varphi(P,Q)}{\partial n(P)} q^{+}(Q) ds(Q) \\ &= -q^{+}(P) + \int_{z_1}^{\infty} \frac{\partial \varphi(P,Q)}{\partial n(P)} q(Q) dx(Q), \end{aligned} \tag{38}$$

where $P \in \Gamma$.

After obtaining the solution of the boundary integral equation under the condition of single-valued displacement, the SIF at the crack tip can be directly calculated using the following equation [33]:

$$K_{III}(a_j) = -\frac{G_1 \alpha}{2} \lim_{Q \to a_j} [\sqrt{2\pi |Q - a_j|} F(Q)], \tag{39}$$

$$K_{III}(b_j) = -\frac{G_1 \alpha}{2} \lim_{Q \to b_j} [\sqrt{2\pi |Q - b_j|} F(Q)], (j = 1, 2, \ldots n), \tag{40}$$

where a_j and b_j are the initial and terminal endpoints of the j-th crack, respectively.

It is quite challenging to ensure that the boundary integral equation derived above meets the displacement single-valued condition and to solve the equation itself. Hence, alternative methods were explored to substitute for direct solution, and extensive research has shown that the BEM is a viable numerical approach [34]. The boundary and cracks were thus divided into $M + N$ linear units (Figures 3 and 4), i.e., $S + \Gamma = \sum_e L_e$, $S = \bigcup_{j=1}^{M} L_j$, and $\Gamma = \bigcup_{j=1+M}^{M+N} L_j$. Each linear unit was then mapped to an interval $-1 \le t \le 1$, and a point, Q, on a cell, L_e, could be represented as:

$$Q = Q_1^e N_1(t) + Q_2^e N_2(t), (|t| < 1 and Q \in \mathrm{L_e}), \tag{41}$$

where Q_1^e and Q_2^e are two tip nodes of the e-th unit and take the following shape functions:

$$N_1(t) = \frac{1}{2}(1 - t),\ N_2(t) = \frac{1}{2}(1 + t). \tag{42}$$

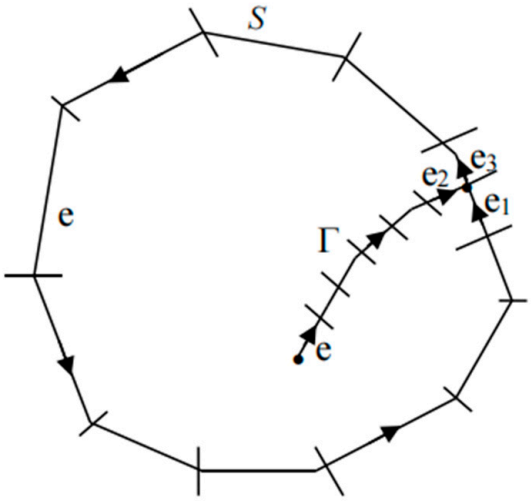


Figure 3. Division of elements on the outer boundaries and cracks (Note: *S* is the outer boundary, Γ is the crack, e_1, e_2, e_3 denote elements on the cracks and boundaries).

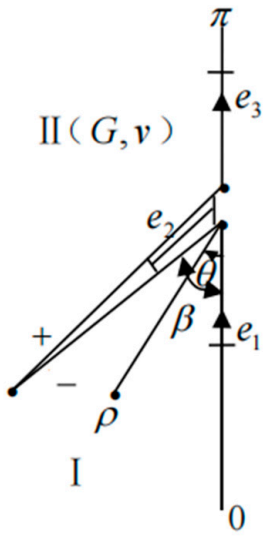


Figure 4. Cell division.

Due to the singularity of the stress field at the crack tip, this study adopted a refinement strategy that combined the local mesh densification and singular elements. Specifically, 1/4-node singular elements were employed in the crack-tip region (a sector area centered at the crack tip with a radius of r = 0.05 D, where the element side length gradually increases outward from the crack tip by a factor of 1.2. This ensured the smallest element size near the crack tip, enabling an accurate capture of the stress singularity. Linear interpolation elements were used for the crack surface and adjacent boundaries, while quadratic interpolation elements were applied at the crack tip to balance the calculation accuracy and efficiency. A gradient-based element division was adopted for the transition between the refined region and the global mesh, avoiding calculation errors caused by mesh distortion. Figure 5 is the schematic representation of the crack-tip element refinement that clearly marks the distribution range of singular elements, element side lengths, and types of interpolation functions.

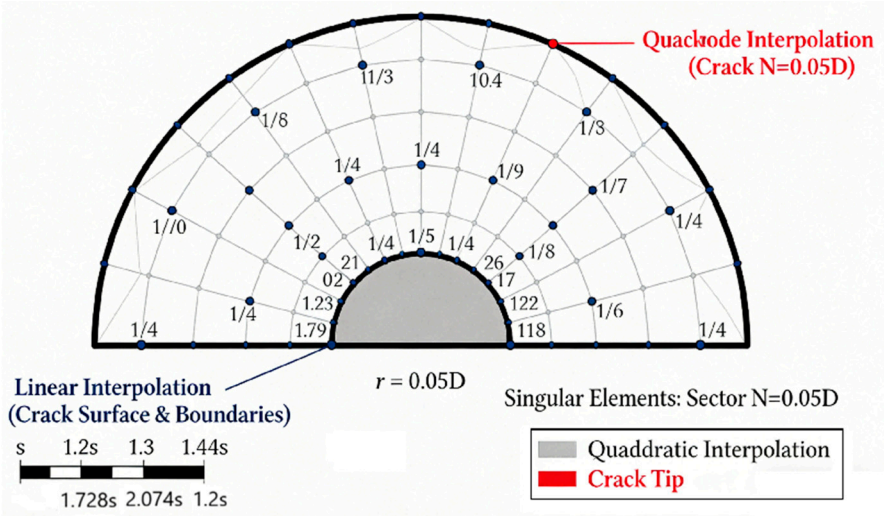


Figure 5. Schematic diagram of crack-tip element refinement.

The interpolation functions on the boundary S and cracks Γ were then defined. The role of the interpolation functions is to ensure the closure of the linear system of equations obtained by discretizing the boundary integral equation and to satisfy the displacement single-valued condition [33]. First, the interpolation functions of the linear elements on the boundary S are defined as follows:

$$F(Q) = F_1^e N_1(t) + F_2^e N_2(t) \ \ (|t| \le 1, Q \in L_e \subset S). \tag{43}$$

Elements along the crack Γ were categorized into general linear elements and crack-tip elements. General linear elements, which exclude the crack tip, had interpolation functions defined as follows:

$$F(Q) = F_1^e N_1(t) + F_2^e N_2(t) \ \ (|t| \le 1, Q \in L_e \subset \Gamma). \tag{44}$$

If the starting node of the cell $t = -1$ was a crack cusp, then $F(Q)$ was represented as:

$$F(Q) = \frac{F_1^e}{\sqrt{N_2(t)}} + (F_2^e - F_1^e) N_2(t) \ \ (|t| \le 1, Q \in L_e \subset \Gamma). \tag{45}$$

Unit e_1 on the boundary S adjacent to the unit e_2, as shown in Figure 4, follows the interpolation function as:

$$F(Q) = (F_1^{e_1} - F_2^{e_1}) N_1(t) + \frac{F_2^{e_1}}{[N_1(t)]^{1-\lambda_1}} \ (|t| \le 1, Q \in L_{e_1} \subset S). \tag{46}$$

For unit e_3 on the boundary S adjacent to the unit e_2, the unknown function $F(Q)$ can be expressed as:

$$F(Q) = \frac{F_1^{e_3}}{[N_2(t)]^{1-\lambda_2}} + (F_2^{e_3} - F_1^{e_3}) N_2(t) \ \ (|t| \le 1, Q \in L_{e_3} \subset S) \tag{47}$$

For the unit e_2 on the crack Γ where the boundary intersects, the following interpolation function was introduced:

$$F(Q) = \frac{F_{2c}^{e_2}}{[N_1(t)]^{1-\lambda_2}} + (F_{1c}^{e_2} - F_{2c}^{e_2} - Q_{2c}^{e_2})[N_1(t)] + \frac{Q_{2c}^{e_2}}{[N_1(t)]^{1-\lambda_1}} \ \ (|t| \le 1, Q \in L_{e_2} \subset \Gamma) \tag{48}$$

On the unit e_1:

$$F(Q) = \frac{\partial \phi(Q)}{\partial s(Q)} = -\frac{\partial \phi(Q)}{\partial \rho}\Big|_{\theta=0} = -\frac{1}{\alpha}\frac{\partial w_1(\rho,0)}{\partial \rho} = -\frac{1}{\alpha}\lambda_1 A_1 \rho^{\lambda_1 - 1} \tag{49}$$

$$F(Q) = (F_1^{e_1} - F_2^{e_1})N_1(t) + \frac{F_2^{e_1}}{[N_1(t)]^{1-\lambda_1}},\ \rho = l_{e_1}N_1(t). \tag{50}$$

hence,

$$\lim_{\rho\to 0}[(\rho)^{1-\lambda_1}F(Q)] = -\frac{1}{\alpha}\lambda_1 A_1 = (l_{e_1})^{1-\lambda_1}F_2^{e_1}. \tag{51}$$

thus,

$$F_2^{e_1} = -\frac{1}{\alpha}\lambda_1 A_1 (l_{e_1})^{\lambda_1 - 1}. \tag{52}$$

On the unit e_2:

$$F(Q) = \frac{\partial \Delta\phi(Q)}{\partial s(Q)} = -\frac{\partial \Delta\phi(Q)}{\partial \rho}\Big|_{\theta=\beta} = -\frac{1}{\alpha}\frac{\partial[w_2(\rho,\beta) - w_1(\rho,\beta)]}{\partial \rho} = -\frac{1}{\alpha}(\lambda_2 C_2 \rho^{\lambda_2 - 1} + \lambda_1 A_1 \rho^{\lambda_1 - 1}) \tag{53}$$

$$F(Q) = \frac{F_{2c}^{e_2}}{[N_1(t)]^{1-\lambda_2}} + (F_{1c}^{e_2} - F_{2c}^{e_2} - Q_{2c}^{e_2})[N_1(t)] + \frac{Q_{2c}^{e_2}}{[N_1(t)]^{1-\lambda_1}},\ \rho = l_{e_2}N_1(t). \tag{54}$$

Hence,

$$\lim_{\rho\to 0}[(\rho)^{1-\lambda_2}F(Q)] = -\frac{1}{\alpha}\lambda_2 C_2 - \frac{1}{\alpha}\lambda_1 A_1 \rho^{\lambda_1 - 1}\rho^{1-\lambda_2} = F_{2c}^{e_2}(l_{e_2})^{1-\lambda_2} + Q_{2c}^{e_2}[N_1(t)]^{\lambda_1 - 1}\rho^{1-\lambda_2}. \tag{55}$$

Then,

$$F_{2c}^{e_2} = -\frac{1}{\alpha}\lambda_2 C_2 (l_{e_2})^{\lambda_2 - 1} \tag{56}$$

$$Q_{2c}^{e_2} = -\frac{1}{\alpha}\lambda_1 A_1 (l_{e_2})^{\lambda_1 - 1}. \tag{57}$$

On the unit e_3:

$$F(Q) = \frac{\partial \phi(Q)}{\partial s(Q)} = \frac{\partial \phi(Q)}{\partial \rho}\Big|_{\theta=\pi} = -\frac{1}{\alpha}\frac{\partial w_2(\rho,\pi)}{\partial \rho} = -\frac{1}{\alpha}\lambda_2 C_2 \rho^{\lambda_2 - 1} \tag{58}$$

$$F(Q) = \frac{F_1^{e_3}}{[N_2(t)]^{1-\lambda_2}} + (F_2^{e_3} - F_1^{e_3})N_2(t),\ \rho = l_{e_3}N_2(t). \tag{59}$$

Hence,

$$\lim_{\rho\to 0}[(\rho)^{1-\lambda_2}F(Q)] = -\frac{1}{\alpha}\lambda_2 C_2 = (l_{e_3})^{1-\lambda_2}F_1^{e_3}. \tag{60}$$

Then,

$$F_1^{e_3} = -\frac{1}{\alpha}\lambda_2 C_2 (l_{e_3})^{\lambda_2 - 1}. \tag{61}$$

Similarly,

$$F_{2c}^{e_2} = (l_{e_2})^{\lambda_2 - 1}(l_{e_3})^{1-\lambda_2}F_1^{e_3} \tag{62}$$

$$Q_{2c}^{e_2} = (l_{e_1})^{1-\lambda_1}(l_{e_2})^{\lambda_1 - 1}F_2^{e_1}. \tag{63}$$

The boundary integral equation for the torsional problem is [33]:

$$\int_{S+\Gamma} \frac{\partial \phi(P,Q)}{\partial s(P)} F(Q) ds(Q) = \int_{S} \frac{\partial \phi(P,Q)}{\partial n(P)} q(Q) ds(Q) - \frac{1}{2} f(P), \ (p(x,y) \in S + \Gamma) \tag{64}$$

The integrals contained within the boundary integral of Equation (64) and the displacement single-valued condition were rewritten as the sum of the integrals of the boundary. The interpolation Equations (43)–(48) were then substituted separately based on the element type. Furthermore, by selecting the source points P in the integral Equation (64) as the mid-nodes of each element and adding the already derived Equations (62) and (63), a closed algebraic system of equations for the undetermined values $\{F_j\}$ of the interpolation functions $F(Q)$ was obtained, and its coefficient matrix was composed of regular integrals and singular integrals. For non-singular integrals, the Gauss–Legendre quadrature equation was directly applied for computation. In cases where the source point $P(x_0, y_0)$ was the mid-node of the integral element L_e, the boundary integral Equation (64) included two singular integrals as follows:

$$\int_{L_e} \frac{\partial \phi(P,Q)}{\partial n(P)} q(Q) ds(Q) = \int_{L_e} \frac{1}{2\pi r^2} [\vec{n}(P) \cdot \vec{Q}(P)] q(Q) ds(Q) = 0, \text{ for } P(x_0, y_0) \in L_e \tag{65}$$

$$\int_{L_e} \frac{\partial \phi(P,Q)}{\partial s(P)} F(Q) ds(Q) = \frac{1}{2\pi} \int_{-1}^{1} F(Q(t)) \frac{dt}{t}, \text{ for } P = \frac{1}{2}(Q_1^e + Q_2^e) \in L_e. \tag{66}$$

By substituting the interpolation Equations (43)–(45) into the above equation, the following singular integral equation was obtained:

$$\int_{-1}^{1} F(Q(t)) \frac{dt}{t} = F_2^e - F_1^e, \ (\text{for a linear unit on a boundary S}, \ L_e \subset S); \tag{67}$$

$$\int_{-1}^{1} F(Q(t)) \frac{dt}{t} = F_2^e - F_1^e, \ (\text{for a general unit } \Gamma \text{on a crack that does not contain a crack tip}, \ L_e \subset \Gamma); \tag{68}$$

$$\int_{-1}^{1} F(Q(t)) \frac{dt}{t} = F_1^e \sqrt{2} \ln(3 - 2\sqrt{2}) + (F_2^e - F_1^e), \ (\text{for the start node element}, L_e \subset \Gamma) \tag{69}$$

For the units e_1, e_2, e_3,when any value was used for β, λ_1, and λ_2 were not natural numbers, hence, Newton's binomial theorem was no longer valid. Thus, we only calculated when $\beta = \pi/2$ at $\lambda_1 = \lambda_2 = 4$. Then:

$$\int_{-1}^{1} F(Q(t)) \frac{dt}{t} = -F_1^{e_1} + \frac{1}{6} F_2^{e_1}, \ (\text{for the unit } e_1 \text{ on the boundary } S, \ L_e \subset S); \tag{70}$$

$$\int_{-1}^{1} F(Q(t)) \frac{dt}{t} = -F_{1c}^{e_2} + \frac{1}{6} F_{2c}^{e_2} + \frac{1}{6} Q_{2c}^{e_2}, \ (\text{for the unit } e_2 \text{ at the intersection of the crack and the boundary}, \ L_e \subset \Gamma); \tag{71}$$

$$\int_{-1}^{1} F(Q(t)) \frac{dt}{t} = -\frac{1}{6} F_1^{e_3} + F_2^{e_3}, \ (\text{for the unit } e_3 \text{ on the boundary } S, \ L_e \subset S). \tag{72}$$

The above algebraic equations can solve $\{F_j\}$, $Q_{2c}^{e_2}$ and λ_i in the unknown function $F(Q)$. Once these unknowns are solved, the SIF and torsional stiffness, D, can be calculated according to the method of Lu, Z.Z. [33], yielding the following result:

$$K_{\mathrm{III}}(a_j) = -\frac{G\alpha}{2}\sqrt{2\pi l_e}F_1^e \tag{73}$$

$$K_{\mathrm{III}}(b_j) = 0, \tag{74}$$

where a_j and b_j represent the initial and terminal endpoints of the j-th crack, respectively.

After discretization, the closed integral equation system involves the calculation of integrals over singular elements and non-singular elements. The integrals over singular elements can be computed analytically [35], while the integrals over non-singular elements can be numerically calculated using the Gauss-Legendre quadrature formula [36].

3. Numerical Example of the Torsional Problem of a Cylinder with an Edge Crack

To demonstrate the correctness and effectiveness of the proposed method, two examples of torsional problems of a cylinder with a straight and a broken edge crack are given in this section.

3.1. Cylinders with Straight Edge Cracks

Figure 6 illustrates the torsion of a cylinder containing a straight edge crack. The crack length is $2c$, the distance from the center of the circle to the midpoint of the straight crack is d, the outer radius of the annular structure is R, and the inner radius is r. The crack was divided into 200 elements, while the outer boundary was divided into 320 elements. To ensure the accuracy of the calculations, a local mesh refinement strategy was adopted near the crack tip, where the element size decreased geometrically. Moreover, the minimum element size was approximately 0.5% of the crack length. By systematically varying the number of global elements, convergence analysis of the dimensionless SIF was performed, as shown in Figure 7. When the number of crack-tip elements increased to approximately 200, the calculated SIF tended to stabilize, with a relative error of less than 0.3% observed between adjacent meshes. This result indicated that the numerical solution achieved good convergence.

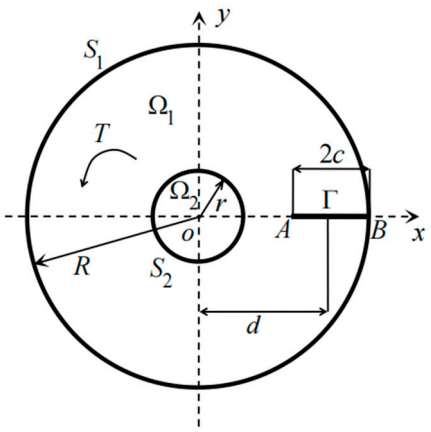


Figure 6. Torsion of a cylinder with a straight edge crack (Note: Ω_1 is the outer circular domain, Ω_2 is the central circular hole domain, T is torque; Γ is the edge crack with length $2c$, R is the radius of the outer circle, r is the radius of the circular hole, and d is the horizontal distance between the crack and the center of the circle).

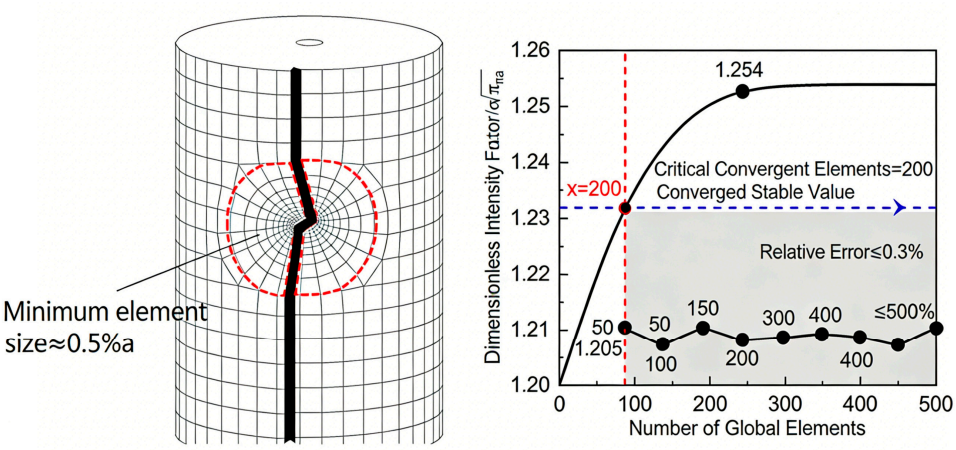


Figure 7. Crack-tip mesh refinement strategy and convergence analysis of the dimensionless stress intensity factor.

Figure 8 shows the changes in the dimensionless SIF $K^*_{\mathrm{III}} = K_{\mathrm{III}}/(G\alpha R\sqrt{\pi c})$ and the dimensionless torsional stiffness $D^* = D/(\frac{\pi}{2}GR^4)$ with the ratio of the edge crack length to the outer cylinder radius $(2c/R)$, where $K^*_{\mathrm{III}}(B) = 0$. These parameters were computed via the Gauss–Chebyshev quadrature method reported in the literature [37], FEM, and the BEM of this study. The computed results were relatively consistent with the results reported in the literature [37], and demonstrated higher accuracy than the FEM results. This demonstrated the effectiveness of the BEM for simulating the singular behavior at crack tips and its suitability for torsion calculations related to cylinders with straight edge cracks.

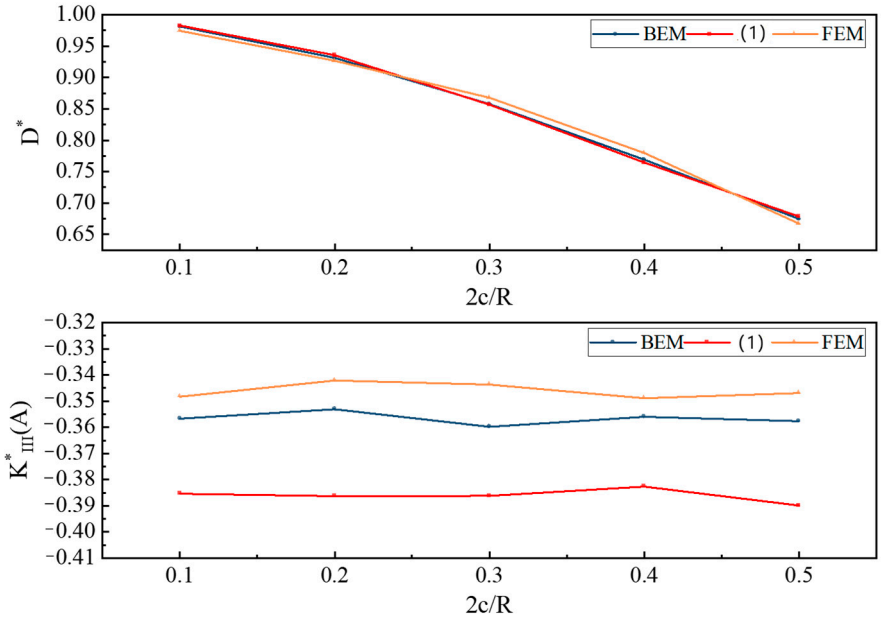


Figure 8. Change of D^* and K^*_{III} of cylinder with straight edge crack with $2c/R$ (r/R = 0.1). Note: (1) in the figure refers to the data from Reference [35].

To quantitatively evaluate the influence of the mesh density on the calculation results, the mesh density sensitivity analysis plot is presented below. The plot shows the sensitivity coefficients and error ranges of each calculation index under different crack lengths, thereby verifying the robustness of the numerical scheme.

Figure 9 shows that when the number of elements varied within the range of 640–960, the dimensionless SIF and torsional stiffness exhibited only slight fluctuations, tending to stabilize at N = 800. This indicated that the mesh scheme adopted in this study had good

stability. The calculation results were insensitive to variations in the mesh density, and the robustness of the numerical method met the requirements of academic research and engineering analyses.

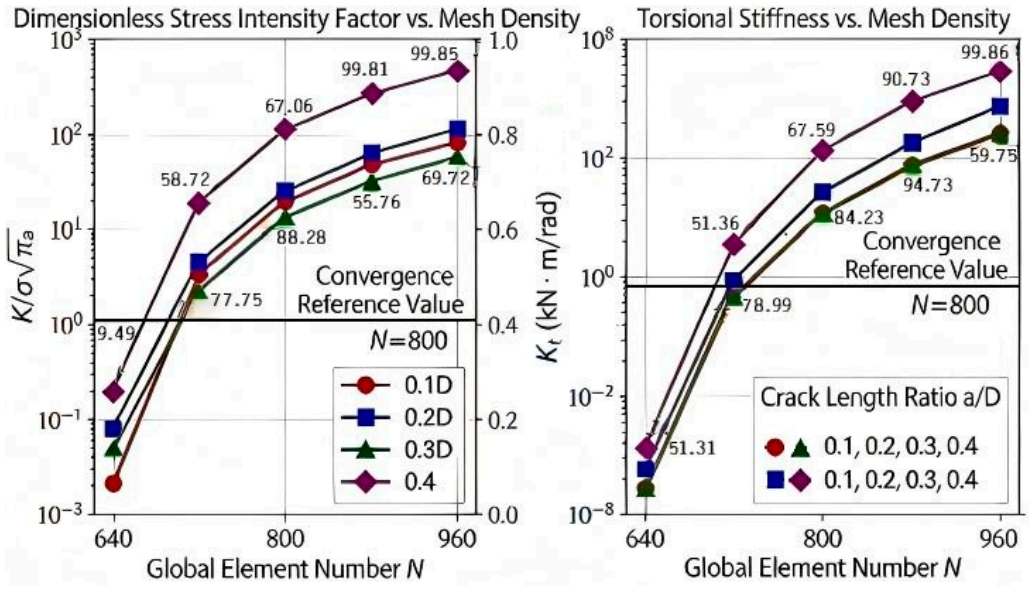


Figure 9. Results of the mesh density sensitivity analysis.

The computation of the dimensionless SIF and torsional stiffness for cylinders with straight edge cracks offers critical quantitative support for the anti-crack design of engineering structures. The SIF acts as a quantitative measure of the stress field strength at the crack tip. It directly determines whether the crack will undergo unstable propagation under loading and functions as an early warning sign for structural fracture damage—the higher its value, the greater the critical risk posed by the crack. The torsional stiffness represents the component's capacity to resist torsional deformation. A reduction in stiffness implies that the component's torsional deformation will increase under the same torque, allowing for the extent to which the crack impairs the structural torsional load-bearing capacity to be quantified and thereby providing a quantitative criterion for residual stiffness assessment. When these two parameters are applied to the tower of a cross-sea suspension bridge, the tower serves as the core component bearing the torsional load of the bridge deck. In the case of construction defects or fatigue cracks during the operational period, the dimensionless SIF proposed in this study, together with the actual material parameters and load conditions of the tower, can be used to rapidly assess whether the crack is likely to enter the propagation phase. In addition, the impact of cracks on the torsional performance of the tower can be assessed using the dimensionless torsional stiffness. This provides guidance for determining the timing of the tower crack repair and formulating reinforcement plans, thus ensuring the long-term operational safety of the cross-sea bridge.

3.2. Cylinders with Cracks at the Broken Edge

Figure 10 illustrates the torsion of a cylinder that contains a broken-line edge crack, as computed in this section. The crack length is $a + c$; the distance from the center of the circle to the crack's inflection point is d; the angle between the broken line and the x-axis is β; the outer radius of the annular structure is R; and the inner radius is r. The crack was divided into 300 elements, while the outer boundary was divided into 400 elements. Figure 11 presents the changes in the dimensionless torsional stiffness D^* and dimensionless SIF $K^*_{\mathrm{III}} = K_{\mathrm{III}}/(G\alpha R\sqrt{\pi(a+c)})$ (computed via the method of this study) with the broken-line angle β, where $K^*_{\mathrm{III}}(B) = 0$. In the specific calculation process, the values $r/R = 0.1$, $a/R = 0.3$,

c/R = 0.1, and d/R = 0.7 were used. The results showed that when the values of β were centered at 0, the distribution on either side was generally symmetric. At $\beta = 0$, the torsional stiffness reached its minimum value, while the SIF reached its maximum value. The computed results further demonstrated that the BEM was equally applicable for the computation of torsion in cylinders with broken-line edge cracks.

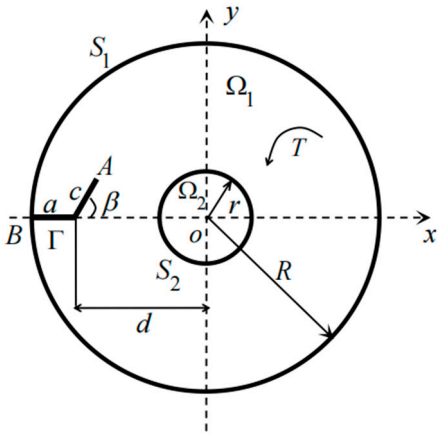


Figure 10. Torsion of a cylinder with a broken edge crack (Note: Γ is the Polygonal edge crack, d is the horizontal distance between the crack and the center of the circle).

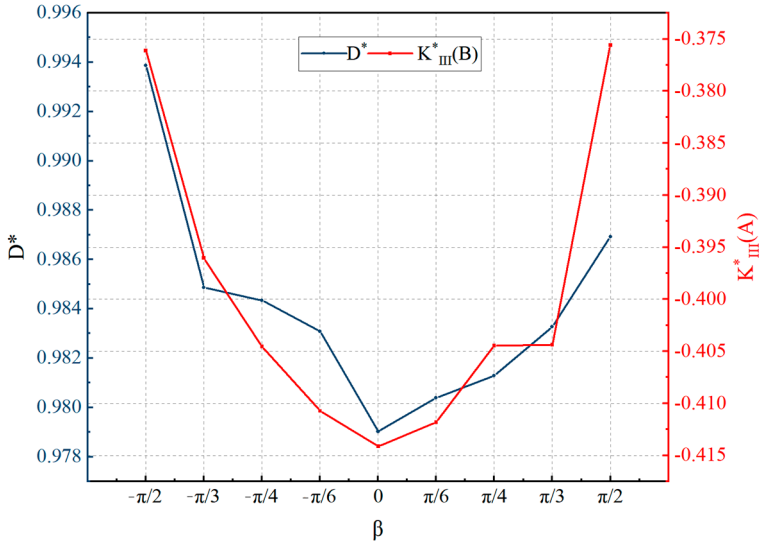


Figure 11. Changes in D^* and K^*_{III} of a cylinder with a broken edge crack with β.

In contrast to simple straight cracks, broken-line cracks tend to generate mixed-mode SIFs more easily due to their geometric discontinuity. This indicates that the stress field at the crack tip is more complex. Instead of propagating in the original direction, the crack may deflect or branch, leading to a less predictable propagation path and potentially higher destructiveness.

The model constructed in this research was subjected to a rigorous mesh independence validation to ensure the accuracy and reliability of the boundary element numerical computation results. The purpose of this analysis is to demonstrate that the key solutions do not rely on the mesh density, thereby ensuring the robustness of the conclusions. We chose a representative calculation working condition as the test case. On this basis, a series of mesh schemes ranging from coarse to fine were generated systematically, with the total number of mesh elements was gradually increased from approximately 50 to 500. Special attention was paid to the mesh quality of the crack area during the mesh division process.

The computation results indicated that as the number of meshes increased, the value of the monitored quantity significantly changed significantly before gradually stabilizing. Once the total number of mesh elements reached 200, further increasing the number of mesh elements to 500 led to a change of merely 0.25% in the monitored quantity, which was well below the preset convergence threshold of 0.5%. Hence, it was concluded that the solution had good independence at this mesh density.

The flowchart of the FORTRAN 2018 program is presented in Figure 12.

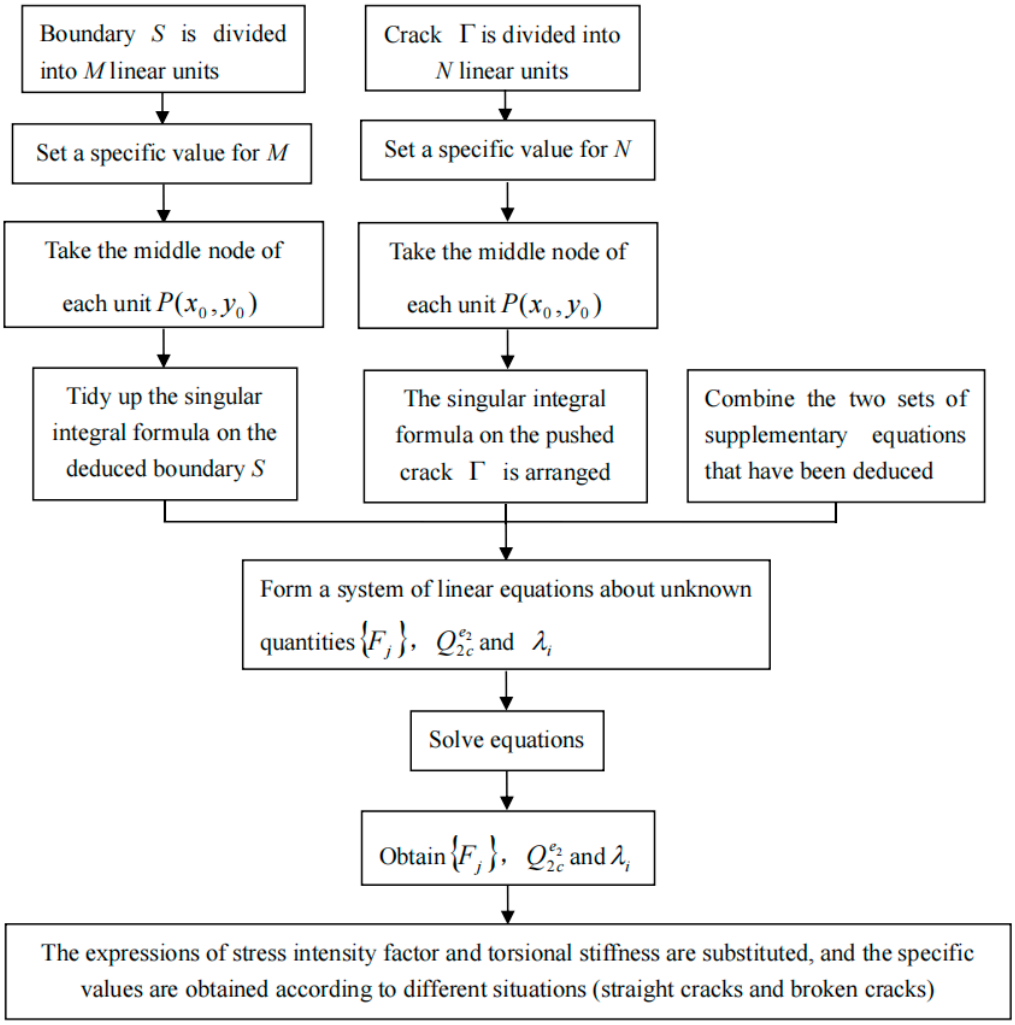


Figure 12. FORTRAN program flow chart.

4. An Example of a Torsional Analysis of Suspension Bridge Towers Under Wind Load

4.1. Torsional Effect of Wind Load on the Tower Column Body

The research object of this study was the reinforced concrete pylon of a cross-sea suspension bridge in China, with a main span of 1288 m and a rhombus-frame structure. The key geometric and performance parameters of the pylon were as follows:

(1) Cross-sectional dimensions of the pylon: The cross-section of the lower pylon column is a circular ring with an outer radius R_0 = 6.5 m, an inner radius R_i = 5.0 m, and a wall thickness of 1.5 m. The cross-section of the upper pylon column tapers gradually to an outer radius R_0 = 4.8 m and an inner radius R_i = 3.8 m.

(2) Height parameters of the pylon: The total height is 215 m, including the lower pylon column of 80 m, a middle pylon column of 105 m, and a upper pylon column of 30 m.

(3) Geometric settings of the cracks: Based on the statistics of the actual pylon construction defects and operational damage, the cracks are set at height of 40 m on the lower pylon column (a torque-concentrated region). The length range of the straight cracks is 0.5–3.0 m, and the turning angles of the zigzag cracks are 15°, 30°, and 45°, which are consistent with the typical distribution characteristics of cracks in practical engineering.

(4) Material properties of the pylon: The main structure of the pylon is made of C50 reinforced concrete, with a modulus of elasticity of E = 3.45 × 104 MPa, a Poisson's ratio v = 0.2, a compressive strength of f_c = 23.1 MPa, and a tensile strength of f_t = 2.64 MPa. For the fracture mechanics parameters, the fracture toughness was K_{IIIc} = 1.5 MPa·m$^{1/2}$ (as measured via the three-point bending test of C50 concrete).

Based on references [38–40], the wind load acting on the tower was calculated using the following equation:

$$F = k \cdot k_z \cdot \beta_z \cdot P_0 \cdot A, \tag{75}$$

where k denotes the shape coefficient of the wind load, i.e., the pressure generated when the wind acts on the building surface, whose magnitude is associated with the building dimensions; and k_z stands for the height-dependent coefficient of the offshore wind pressure, which increases with height above the sea level; β_z denotes the wind oscillation coefficient; P_0 denotes the fundamental wind pressure; and A refers to the outline projection area of the component that is perpendicular to the wind direction.

As illustrated in Figure 13, the pylons of the cross-sea suspension bridges were subjected to vertical pressure from the main cables throughout the year, along with long-term fluctuating torsional loads induced by wind, seismic activity, and vehicle loads. In particular, during typhoon events, the interaction between unbalanced live loads on either side of the main cables and strong wind loads results in considerable torque in the lower section of the pylon, particularly in the pylon columns.

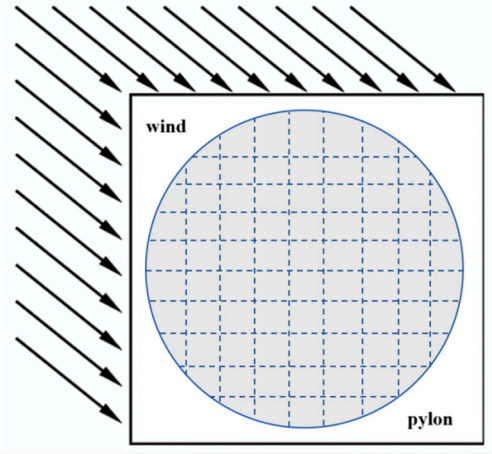


Figure 13. Top view of the pylon under wind action.

4.2. Example of the Numerical Calculation for the Pylon Column

In this section, the torsional fracture of the suspension bridge pylon column with a straight edge crack is computed under different wind loads conditions. The pylon column segment was treated as a simplified cylinder made of high-strength concrete and containing a straight edge crack. To achieve an accurate analysis of the torsion problem of suspension bridge pylons with edge cracks under wind loads while balancing the operability of mechanical modeling and computational efficiency, we simplified the primary force-bearing section of the pylon into a uniform-section cylinder made of high-strength

concrete with straight edge cracks. This simplification was based on three key assumptions and a corresponding rationality verification: (1) in terms of the geometric shape, the local structural details, such as construction joints, were neglected; (2) in terms of the material properties, the pylon was regarded as a homogeneous isotropic material; and (3) in terms of the crack morphology, the cracks were simplified as straight through cracks. For the rationality verification, a comparison with the prototype of a C50 high-strength concrete pylon of a suspension bridge with a main span of 1200 m showed that the deviations of the section moment of inertia and torsional moment of inertia between the simplified model and the prototype were 3.2% and 4.1%, respectively. The errors of the torsional stiffness and SIF were both less than 4% for cases without cracks and for cases with 50 mm cracks. Moreover, the consistency with mainstream domestic and foreign studies, as well as engineering practice of a cross-sea bridges, confirmed the effectiveness of this simplification [41–44]. It should be noted that this model is applicable to a linear elastic torsion analysis of the main force-bearing section of the pylon, and secondary corrections can be introduced through relevant correction coefficients for extreme working conditions. With the wind loads applied, a numerical computation program was developed using the aforementioned data in accordance with the BEM recommended in this study. This resulted in the dimensionless torsional stiffness and SIF being as follows:

$$D* = 0.996652,\ K^*_{\mathrm{III}}(A) = -0.597362,\ K^*_{\mathrm{III}}(B) = 0. \tag{76}$$

The strain energy density factor criterion for pure type III cracks is given in [45–47]:

$$K_{\mathrm{III}c} = \sqrt{1-2\nu}K_{\mathrm{I}c} = 0.816K_{\mathrm{I}c} = 0.90168(MN/m^{3/2}),\ (\nu = 0.167). \tag{77}$$

Wind speeds corresponding to various wind grades were acquired through reviewing an extensive range of literature. In accordance with the fracture criterion, $K_{\mathrm{III}} \leq K_{\mathrm{IIIC}}$, the maximum permissible crack length of the cylindrical portion of the suspension bridge pylon with straight edge cracks under different wind load actions was computed. These results are illustrated in Figure 14.

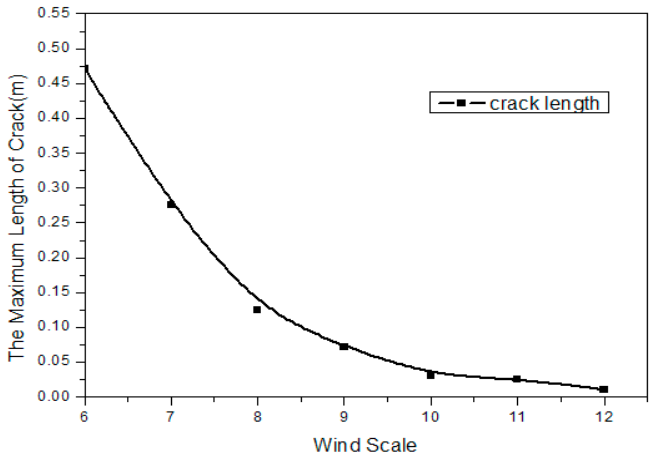


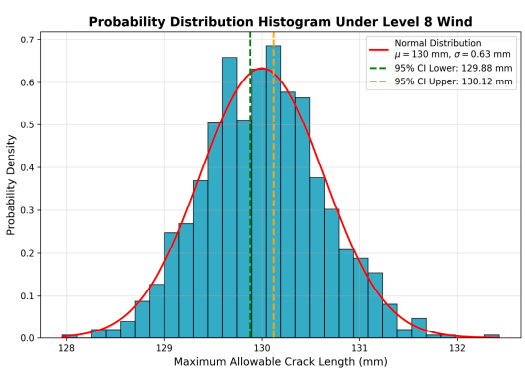
Figure 14. Variation in the maximum allowable crack length of the cracked pylon column under various wind grades.

It can be observed from the figure that, as the offshore wind load increases, the maximum permissible crack length of the cracked cylinder pylon column steadily decreases. This critical value not only directly governs the operational safety of the bridge, but also has a far-reaching influence on the long-term design as well as operation and maintenance strategies.

It is worth noting that treating the maximum allowable crack length as a deterministic threshold has inherent limitations. Therefore, we conducted an uncertainty analysis based on the Monte Carlo simulation. The key uncertain factors were selected as follows:

(1) Core material parameters of the pylon: The tensile strength (assumed to follow a normal distribution with a mean of 2.64 MPa and a coefficient of variation of 0.05); and the elastic modulus (assumed to follow a normal distribution with a mean of 3.45×10^4 MPa and a coefficient of variation of 0.03);
(2) Peak wind load under different wind levels (assumed to follow a lognormal distribution, with parameters determined based on Specification GB 50009-2012 [48] and field measurement data);
(3) Crack size measurement error (assumed to follow a uniform distribution with an error range of ± 0.02 mm).

Through 1000 random samplings, the maximum allowable crack length corresponding to each sampling group was calculated using the BEM, and the corresponding probability distribution histograms and statistical parameter tables were obtained. Wind level 8 was used as the representative wind condition (as shown in Figure 15). Under this condition, the maximum allowable crack length had a mean of 130 mm, a standard deviation of 0.63 mm, and a 95% confidence interval of [129.88, 130.12] mm. These results indicated that the maximum allowable crack length was not a fixed threshold but followed a well-defined probability distribution, which effectively compensated for the limitations of a purely deterministic analysis.



Statistical Parameter Table Under Level 8 Wind

Statistical Indicator	Value	Unit
Sample Size	1000	-
Mean (μ)	130.00	mm
Standard Deviation (σ)	0.63	mm
Minimum Value	127.96	mm
Maximum Value	132.43	mm
Median	130.02	mm
Variance	0.3806	mm²
Coefficient of Variation	0.48	%
95% CI Lower Bound	129.88	mm
95% CI Upper Bound	130.12	mm

Figure 15. Probability distribution and statistical parameters of the maximum allowable crack length for the edge-cracked pylon column under Level 8 wind conditions.

In terms of safety, the critical crack length serves as a key threshold at which the structure shifts from a damaged condition to failure. As the primary load-bearing component of a suspension bridge, the pylon sustains a substantial axial force and, at the same time, is subjected to bending moments induced by wind loads and seismic activities, which tend to result in significant stress concentration at the crack tip. The computed critical crack length represents the precise turning point for unstable crack propagation under the most adverse load combination. If the actual crack length approaches or exceeds this threshold, a brittle fracture may occur in the pylon body. This leads to sudden changes in structural stiffness, imbalance in the internal force redistribution, and potentially a chain reaction involving pylon failure and main cable malfunction, which ultimately jeopardize the safety of the entire bridge. Hence, this result provides a critical basis for assessing the remaining service life of the structure and for implementing early risk warnings. To comply with the safety design requirements of practical bridge engineering while considering the pylon as a Class-I critical component, safety factor calibration and threshold correction were supplemented. We referred to the safety reserve requirements for brittle fracture

components specified in the General Code for Design of Highway Bridges and Culverts (JTG D60-2015 [49]). We then used the maximum allowable crack length obtained in this study as the baseline, and a safety factor of 1.2 was applied by accounting for the brittle characteristics of the crack propagation and the core load-bearing role of the pylon. This value ensures adequate safety reserves while avoiding excessive conservatism that would lead to unnecessary engineering costs. The corrected threshold values corresponding to different wind grades are presented in Figure 16.

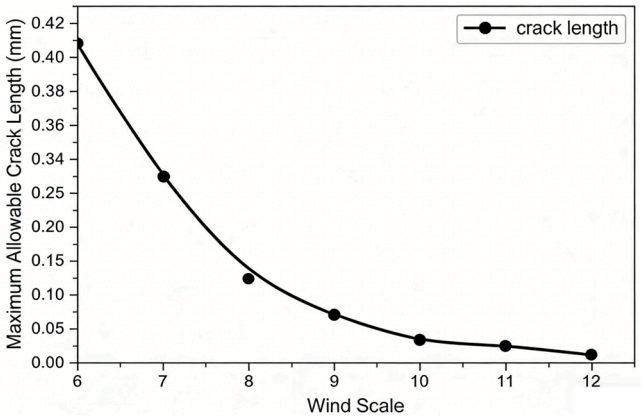


Figure 16. Variation in the corrected maximum allowable crack length for the cracked pylon columns (with a safety factor of 1.2) with wind scale.

The corrected maximum allowable crack length provides an explicit quantitative criterion for bridge health monitoring and periodic inspection at the operational and maintenance (O&M) management level. The core value of this lies in scientifically defining the thresholds for crack alarm and repair, thereby equipping the formulation of inspection cycles and maintenance decision-making with a reliable quantitative foundation. This ensures that cracks are identified in a timely manner and addressed prior to propagating to a critical state. Based on this engineering threshold, we further developed a three-level inspection early-warning standard as follows:

(1) Low-risk level: When the measured crack length is less than 0.5 times the corrected threshold, a routine inspection cycle (once every two years) is adopted.
(2) Medium-risk level: When the measured crack length ranges from 0.5 times the corrected threshold to the corrected threshold, the inspection cycle is shortened to once per year, with simultaneous enhancement of real-time monitoring.
(3) High-risk level: When the measured crack length reaches or exceeds the corrected threshold, it is imperative to immediately suspend operation, conduct a comprehensive inspection, and formulate a targeted reinforcement scheme.

This hierarchical standard transforms bridge operation and maintenance from a passive response mode to an active prevention mode, facilitating the upgrade of O&M strategies toward refined and predictive management.

5. Conclusions

This study focuses on the torsional behavior of edge-cracked pylon cylinders of suspension bridges under wind loads. Through a combination of theoretical analysis and numerical simulation, the key mechanical characteristics of pylon torsional fracture and the engineering application potential of the BEM are systematically investigated. The main conclusions are drawn as follows:

(1) Based on the torsion theory of elastic mechanics, boundary integral equations for edge-cracked cylinders were established, which clarified the singularity characteristics of the stress field at crack tips. This research addresses the deficiency of insufficient theoretical analysis of wind-induced torsional fracture in suspension bridge pylons in existing studies, providing a solid theoretical basis for the accurate calculation of SIFs for such problems.
(2) A BEM-based numerical algorithm tailored for the torsional fracture analysis of pylons was proposed. Through rational boundary element division and the selection of multiple forms of interpolation functions, high-precision calculations of torsional stiffness and SIFs for cylinders with straight or polygonal edge cracks were achieved. Verification against theoretical solutions and experimental data reported in the literature confirms that the proposed algorithm exhibits high accuracy and reliability. The method fully leverages the advantages of BEM in handling crack-related discontinuities and accurately captures crack-tip singularities, thereby filling the gap in the application of BEM in the field of torsional fracture analysis of bridge pylons.
(3) Numerical simulations under different wind load conditions were performed, which quantified the effects of crack length, crack form (straight or polygonal), and wind load grade on the attenuation of torsional stiffness and the evolution of SIFs at crack tips in pylon cylinders. The maximum allowable crack length thresholds under various wind grades were determined, which were directly correlated with the local crack damage in pylons under actual wind load conditions in engineering practice, thereby providing a quantitative basis for damage assessment and safety early warning of suspension bridge pylons.

In summary, this study systematically reveals the torsional fracture mechanism of edge-cracked pylon columns of suspension bridges under wind loads, improves the theoretical framework for torsional fracture analysis of bridge structures, and verifies the engineering applicability of BEM in torsional fracture analysis of pylon engineering. The research findings not only provide direct technical support for the wind-resistant design and damage detection of suspension bridge pylons, but they can also be extended to the overall bridge safety evaluation system. By quantifying the influence of local cracks in pylons on main cable displacement and deck stability, a multilevel safety evaluation logic from the local to global levels is established, which ultimately provides systematic and comprehensive theoretical and technical support for the full life-cycle safety management of cross-sea suspension bridges.

It should be noted that the simplification of pylon cracks as single edge cracks in this study is intended to eliminate complex interfering factors, focus on the core mechanical mechanism by which cracks affect the torsional bearing capacity of pylons, and prioritize verification of the validity of fundamental theories and numerical calculation methods (e.g., the reliability of the BEM is verified by comparing with results reported in the existing literature), thereby laying a solid foundation for subsequent research on complex crack problems. In future work, the calculation method for the maximum allowable crack length proposed in this study can be further expanded and optimized by introducing multicrack interference theory and adjusting the calculation parameters based on the actual crack morphology obtained from field inspection. These improvements will enhance the applicability of the method to complex crack scenarios in practical engineering, thus providing more accurate technical references for evaluating the safety of actual pylons.

Author Contributions: Validation, Q.D.; writing—original draft, N.L. and K.Z.; writing—review and editing, J.G.; data curation—C.W.; formal analysis—X.Y.; resources—H.Y.; Methodology and Software—L.Z. All authors have read and agreed to the published version of the manuscript.

Funding: This research was funded by the Science and Technology Program of Shandong Provincial Department of Transportation—Durability Assessment and Service Life Prediction of Rushankou Bridge Based on a Multi-source Data Artificial Intelligence Large Model, grant number (2025BAI14-01).

Data Availability Statement: The original contributions presented in this study are included in the article. Further inquiries can be directed to the corresponding author.

Acknowledgments: Thanks to Yinbang Wang, the supervisor of the first author, for his previous guidance on the derivation of the formulas in this paper.

Conflicts of Interest: The authors declare no conflicts of interest.

Nomenclature

Table presents the explicit definitions and physical meanings of all symbols, variables, and parameters employed in this study.

№	Symbols, Variables, and Parameters	Definition and Physical Meaning	№	Symbols, Variables, and Parameters	Definition and Physical Meaning
1	u	X-direction Displacement	22	n	Unit Normal Vector of the Outer Normal
2	v	Y-direction Displacement,	23	T	Torsional Moment Acting on the End Face
3	w	Z-direction Displacement	24	$\phi(x,y)$	Torsion Stress Function
4	x		25	Γ	crack
5	y	The three XYZ coordinate axes	26	$P(x,y)$	Source Point $P(x,y) \in \Omega$
6	z		27	$Q(\xi,\eta)$	Field Point $Q(\xi,\eta) \in S+\Gamma$
7	ϕ	Torsion Function	28	$F(Q)$	Solution to the Boundary Integral Equation
8	G	Shear Modulus	29	$K_{\mathrm{III}}(a_j)$	Stress Intensity Factor at the Initial Endpoint of the j-th Crack
9	α	Torsion Rate	30	$K_{\mathrm{III}}(b_j)$	Stress Intensity Factor at the Terminal Endpoint of the j-th Crack
10	z	Location of the Cross-Section	31	K^*_{III}	Dimensionless Stress Intensity Factor
11	ρ	Polar Coordinates	32	$N_1(t), N_2(t)$	Shape Function
12	θ		33	e_1, e_2, e_3	Elements on the Cracks and Boundaries
13	ε	Strain	34	L_e	Integration Element
14	γ	Shear Strain	35	R	Outer Radius of the Circular Ring
15	λ	Period of Trigonometric Functions	36	r	Inner Radius of the Outer Circular Ring
16	τ	Shear Stress	37	D	Torsional Stiffness
17	A, B	Coefficients in Front of Trigonometric Functions	38	D^*	Dimensionless Torsional Stiffness
18	k	Multiple	39	c	Crack Length
19	β	Angle	40	M, N	Linear Element
20	Ω	Cross-Section	41	$P(x_0,y_0)$	Midnode of Each Element
21	S	Cross-Section Boundary			

References

1. Hu, J.; Zhang, X.; Tan, S.; Liang, Y.; Wang, J. Fatigue Damage Analysis of Steel Truss Suspension Bridge Under Non-Stationary and Non-Gaussian Buffeting. *Int. J. Struct. Stab. Dyn.* **2025**, *25*, 2550055. [CrossRef]
2. Mao, J.X.; Gui, G.; Wang, H.; Nie, J.H.; Zong, H.; He, X.P. Field measurement research on dynamic performance of steel pylon of a long-span cable-stayed bridge under typhoons. *China J. Highw. Transp.* **2023**, *36*, 101–112.
3. Lei, W.; Wang, Q.; Liao, H.; Li, Z. Vortex-induced vibration characteristics and mechanisms of portal steel bridge tower. *J. Vib. Shock.* **2024**, *43*, 1–8.
4. Wang, F.; Ding, M.; Si, W.; Lu, J. Sand erosion of steel-concrete composite girder cable-stayed bridge is considered time-varying seismic vulnerability analysis. In Proceedings of the 2024 7th International Conference on Civil Architecture, Hydropower and Engineering Management (CAHEM 2024), Kunming, China, 27–29 September 2024.
5. Shen, G.H.; Li, B.H.; Guo, Y.; Zhao, Z.; Pan, F. Calculation methods of torsion response and torsion equivalent static wind loading of transmission tower. *J. Zhejiang Univ. (Eng. Sci.)* **2022**, *56*, 579–589.
6. Zhang, H.S.; Tan, D.P.; Xu, S.C.; Hu, T.; Qi, H.; Li, L. Investigation of Crack Propagation and Failure of Liquid-Filled Cylindrical Shells Damaged in High-Pressure Environments. *J. Mar. Sci. Eng.* **2024**, *12*, 921. [CrossRef]

7. Zhou, Y.; Sun, Y.; Li, M. Experimental Research on Wind Resistant Performance of Free Standing Pylon of Long-Span Cable-Stayed Bridge. *Bridge Constr.* **2020**, *50*, 52–57.
8. Zhang, Q.; Feng, Z.; Zhao, C. Research on Wind-resistance of the Steel-concrete Composite Pylon for Single Cable-plane Bridge during Construction. *Highway* **2013**, *9*, 286–292.
9. Zhang, T.; Zhu, Z.; Zhang, F. Dynamic mode I fracture behavior of frozen soil under impact loading and FDEM numerical simulation: Based on a rate-dependent elastoplastic and cohesive model. *Theor. Appl. Fract. Mech.* **2025**, *141*, 105261. [CrossRef]
10. Wang, D.H.; Li, S.; Sun, C. Assessment of wind-induced fragility of transmission towers under quasi-static wind load. *Wind. Struct.* **2021**, *33*, 343–352.
11. Niu, Z.; Zhu, Z.; Que, X.; Xie, X.; Jin, K. Experimental study on damage evolution process, seepage characteristics, and energy response of columnar jointed basalt under true triaxial cyclic loading. *Geoenergy Sci. Eng.* **2024**, *237*, 212774. [CrossRef]
12. Wang, Y.; Cao, Z.; Li, P.; Yi, X. On the fracture and energy characteristics of granite containing circular cavity under variable frequency-amplitude fatigue loads. *Theor. Appl. Fract. Mech.* **2023**, *125*, 103872. [CrossRef]
13. Liang, J.-T.; Shang, L.-H.; Han, T. Research on crack detection and cause analysis of cable tower cracks in cross sea cable-stayed bridges. *Constr. Mach.* **2024**, *6*, 168–178. [CrossRef]
14. Li, Q.; Xue, Y.-D.; Liu, T. Dynamic Fracture Experimental Study on Cantilever Beam with Prefabricated Cracks. *Sci. Technol. Eng.* **2018**, *18*, 309–314.
15. Wang, X.; Li, X.-G.; Yan, K.-Y. Finite Element Simulation of Vibration Damage of Curved Tower Cable-Stayed Bridge with Spatial Torsion Cable Plane. *Comput. Simul.* **2024**, *41*, 101–105.
16. Dai, K.; Zhao, Z.; Mao, Z. Failure of a wind turbine tower under extreme dynamic loads. *J. Vib. Shock.* **2019**, *38*, 252–272.
17. Li, J.-Y.; Zhou, F.-J.; Lu, J.-H. Modified IWAN model of helical threaded connector imposed to torsional load. *J. Jilin Univ. (Eng. Technol. Ed.)* **2023**, *53*, 1305–1314.
18. Rocha, M.; Trevelyan, J.; Leonel, E.D. An extended isogeometric boundary element formulation for three-dimensional linear elastic fracture mechanics. *Comput. Methods Appl. Mech. Eng.* **2024**, *423*, 116872. [CrossRef]
19. Dong, J.; Ha, J.; Ge, S. Stability Analysis of Concrete Filled Steel Tube Cable-stayed Bridge with Single Tower and Double Cable Planes. *Constr. Technol.* **2022**, *51*, 60–69.
20. Zvyagin, A.V.; Udalov, A.S.; Shamina, A.A. Boundary element method for investigating large systems of cracks using the Williams asymptotic series. *Acta Astronaut.* **2022**, *194*, 480–487. [CrossRef]
21. Civera, M.; Rosso, M.M.; Marano, G.C.; Chiaia, B. Validation and Comparison of Two AOMA Approaches for the Ambient Vibration Testing of Long Suspension Bridges Under Strong Wind Loads. In Proceedings of the 10th International Operational Modal Analysis Conference (IOMAC), Naples, Italy, 21–24 May 2024.
22. Rosso, M.M.; Civera, M.; Dessena, G.; Chiaia, B.; Marano, G.C. Experimental Damping Identification of a Bridge Case Study in Norway under Still Air Conditions. In Proceedings of the 11th International Operational Modal Analysis Conference-IOMAC, Rennes, France, 20–23 May 2025.
23. Li, Z.; Zhang, Z.; Wang, T. Wind-induced collapse fragility analysis of double column suspended guyed tower. *J. Cent. South Univ. (Sci. Technol.)* **2024**, *55*, 255–267.
24. Liu, G.; Lu, B.; Song, H. Study on Wind-induced Structural Internal Force Response of Xihoumen Bridge Pyon. *J. Highw. Transp. Res. Dev.* **2009**, *26*, 64–68.
25. Zhang, S.; Xu, W.; Yao, T. Research on cracking risk of cable tower concrete based on multi-field coupling. *Concrete* **2020**, *6*, 37–40.
26. Lee, Y.-T.; Chen, J.-T.; Kuo, S.-R. Semi-analytical approach for torsion problems of a circular bar containing multiple holes and/or cracks. *Eng. Fract. Mech.* **2019**, *219*, 106547. [CrossRef]
27. Yin, R.-T.; Zhu, B.; Yuan, S.-W. Dynamic analyses of long-span cable-stayed and suspension cooperative system bridge under combined actions of wind and regular wave loads. *Appl. Ocean. Res.* **2023**, *138*, 103683. [CrossRef]
28. Yu, H.; Zhang, M.; Chen, T. Research on wind resistance performance of a pipeline suspension bridge without wind cable in natural wind. *Eng. Struct.* **2025**, *335*, 120320. [CrossRef]
29. Hao, J.M.; Wu, T. Downburst-induced transient response of a long span bridge: A CFD-CSD-based hybrid approach. *J. Wind Eng. Ind. Aerod.* **2018**, *179*, 273–286. [CrossRef]
30. Brebbia, C.A. *Boundary Element Techniques*; Springer: Berlin/Heidelberg, Germany, 1978.
31. Anderson, T.L. *Fracture Mechanics: Fundamentals and Applications*, 3rd ed.; CRC Press: Boca Raton, FL, USA, 2005; pp. 154–196.
32. Kandpal, S.; Bora, S.N. Analytical Solution for Linearized Saint-Venant Equations with a Uniformly Distributed Lateral Inflow in a Finite Rectangular Channel. *Water Resour. Manag.* **2023**, *37*, 5655–5676. [CrossRef]
33. Lu, Z.Z. A new boundary method for torsion problems of bars with curvilinear cracks. *J. Eng. Mech.* **2007**, *24*, 41–46.
34. Dai, Y.; Li, H.; Liu, B.; Yang, C. Calculation boundary vulnerability of numerical algorithm in milling stability prediction. *Int. J. Adv. Manuf. Technol.* **2022**, *119*, 8271–8286. [CrossRef]
35. Maksymovych, M.O.; Kharchenko, Y.V. Determination of Stresses in an Anisotropic Strip with Holes by Using Singular Integral Equations and Green's Solution. *J. Math. Sci.* **2023**, *273*, 79–91. [CrossRef]

36. Borachok, I.; Palianytsia, O.; Chapko, R. Method of Radial Basis Functions for Solving the Partial Integro-Differential Equation of Diffusion with Nonlocal Effects. *Cybern. Syst. Anal.* **2024**, *60*, 621–632. [CrossRef]
37. Tang, R. Saint-Venant torsion of cracked Cylinder. *Chin. J. Mech. Eng.* **1982**, *4*, 332–340.
38. Tang, H.; Yue, M.; Yan, Y.; Li, Z.H.; Li, C.; Niu, K.L. Influence of Soil–Structure Interaction Models on the Dynamic Responses of An Offshore Wind Turbine Under Environmental Loads. *China Ocean Eng.* **2023**, *37*, 218–231. [CrossRef]
39. Li, X.; Dai, G.; Zhu, M.; Wang, L.; Liu, H. A Simplified Method for Estimating the Initial Stiffness of Monopile—Soil Interaction Under Lateral Loads in Offshore Wind Turbine Systems. *China Ocean Eng.* **2023**, *37*, 165–174. [CrossRef]
40. Chauhan, B.S.; Ahuja, A.K.; Chakrabarti, A. Study of Variation in Wind Loads on Rectangular Cross-section Tall Building due to Change in Location of Interfering Buildings. *Arab. J. Sci. Eng.* **2023**, *48*, 12825–12844. [CrossRef]
41. Fang, Y.; Wang, Y.; Yang, H.; Dai, H.; Yan, S. Research progress and bearing capacity calculation model of concrete-filled circular steel tubes under complex loads involving torsional loads. *J. Southeast Univ. (Nat. Sci. Ed.)* **2025**, 1–16.
42. Liu, N. Analysis of the Fracture of Offshore Platform Structures. Ph.D. Thesis, Ocean University of China, Qingdao, China, 2013.
43. Su, Y.-M.; Qing, L.-B. Analytical Methods for Fracture of Concrete Three-point Bending Beams and Theoretical Characteristics of Fracture Process Zone. *Eng. Mech.* **2025**, 1–12.
44. Zhang, H.; Wu, J.; Huang, Y.; Dong, Y.; Peng, C.; Wu, S.; Xu, S. Multiscale Investigation on Damage and Fracture Mechanisms of 3D Printing Ultra-High Performance Concrete under Compression. *J. Chin. Ceram. Soc.* **2025**, *53*, 3313–3328.
45. Torabi, A.R.; Ayatollahi, M.R.; Berto, F.; Razavi, N. Experimental Verification of the Averaged Strain Energy Density Criterion for Brittle Fracture in Blunt V-Notches Under Pure Compression. *Strength Mater.* **2022**, *54*, 1–13. [CrossRef]
46. Liu, J.; Wang, J.; Wu, K.; Yi, X.; Hua, F.; He, Y.; Zhao, H. Multiaxial notch fatigue probability modeling based on three-parameter Weibull distribution and effective strain energy density. *J. Braz. Soc. Mech. Sci. Eng.* **2023**, *45*, 404. [CrossRef]
47. Wu, Y.; Bao, C.; Cai, L.; Wang, K.; Liu, X. Estimation of Fracture Toughness for A508-III Steel in Ductile-to-Brittle Transition Region Using a Strain-Energy–Density-Based Fracture Failure Model. *Acta Mech. Solida Sin.* **2022**, *35*, 834–841. [CrossRef]
48. *GB 50009-2012*; Load Code for the Design of Building Structures. China Architecture & Building Press: Beijing, China, 2012.
49. *JTG D60-2015*; General Code for Design of Highway Bridges and Culverts. China Communications Press Co., Ltd.: Beijing, China, 2015.

Disclaimer/Publisher's Note: The statements, opinions and data contained in all publications are solely those of the individual author(s) and contributor(s) and not of MDPI and/or the editor(s). MDPI and/or the editor(s) disclaim responsibility for any injury to people or property resulting from any ideas, methods, instructions or products referred to in the content.